Journal of The Electrochemical Society, **147** (8) 2910-2922 (2000)
S0013-4651(00)02-015-2 CCC: $7.00

Thermal-Electrochemical Modeling of Battery Systems

W. B. Gu* and C. Y. Wang,z**

GATE Center for Advanced Energy Storage, Department of Mechanical and Nuclear Engineering, The Pennsylvania State University, University Park, Pennsylvania 16802, USA

A general form of the thermal energy equation for a battery system is derived based on first principles using the volume-averaging technique. A thermal-electrochemical coupled modeling approach is presented to simultaneously predict battery electrochemical and thermal behaviors. This approach couples the thermal energy equation with the previous multiphase micro-macroscopic electrochemical model via the heat generation and temperature-dependent physicochemical properties. The thermal-electrochemical model is multidimensional and capable of predicting the average cell temperature as well as the temperature distribution inside a cell. Numerical simulations are performed on a Ni-MH battery to demonstrate the significance of thermal-electrochemical coupling and to investigate the effects of thermal environment on battery electrochemical and thermal behaviors under various charging conditions.

Manuscript submitted February 3, 2000; revised manuscript received May 8, 2000.

As a follow-up of previous work,[1,2] the present work is intended to develop a thermal and electrochemical coupled model capable of predicting the spatial distribution and temporal evolution of temperature inside a battery. It is known that temperature variations inside a battery may greatly affect its performance, life, and reliability. Battery physicochemical properties are generally strong functions of temperature. For example, the equilibrium pressure of hydrogen absorption-desorption, which significantly affects the open-circuit potential of the metal hydride electrode and hence the performance of nickel–metal hydride batteries, is strongly dependent on temperature.[3] Capacity losses occur at low temperatures due to high internal resistances and at high temperatures due to rapid self-discharge.[4] Therefore, a proper operating temperature range is essential for a battery to achieve optimal performance. In order to prolong the battery cycle life, balanced utilization of active materials is desired, which requires a highly uniform temperature profile inside the battery to avoid localized degradation. More important, the battery temperature may increase significantly due to the self-accelerating characteristics of exothermic side reactions such as oxygen reactions in aqueous batteries, eventually causing thermal runaway.[5-8] An optimal operating range and a high uniformity in the internal temperature distribution constitute two thermal requirements for a battery to operate safely. These two are particularly important for advanced electric-vehicle batteries because of their high energy and power densities, large size, and high charge and discharge rates.

Although experimental testing and microcalorimetric measurement[9-11] are necessary to obtain battery thermal data for design and optimization, a mathematical model based on first principles is capable of providing valuable internal information to help optimize the battery system in a cost-effective manner.

In general, a battery thermal model is formulated based on the thermal energy balance over a representative elementary volume (REV) in a battery. The differential equation that describes the temperature distribution in the battery takes the following conservation form[12,13]

$$\rho c_p\left(\frac{\partial T}{\partial t} + \mathbf{v}\cdot\nabla T\right) = \nabla\cdot\lambda\nabla T + q \qquad [1]$$

accumulation convection conduction heat generation

where T is the temperature, $\mathbf{v}$ is velocity vector of the electrolyte, q is the volumetric heat generation rate, and ρ, c_p, and λ are the volume-averaged density, specific heat, and heat conductivity of the REV, respectively. The thermophysical properties can be anisotropic due to the inhomogeneity of battery components.

In batteries with flowing electrolytes, the convection term plays an important role. However, it can be neglected in most stationary batteries, and then Eq. 1 is reduced to the transient heat conduction equation. Subject to proper boundary conditions, Eq. 1 and its various simplified forms have been solved to obtain the temperature distribution in lead-acid,[14-16] nickel-hydrogen,[17] lithium-polymer,[18-21] and lithium-ion[8,22] battery modules, with a single cell as the minimum REV. When the lumped-parameter approach is applicable (cf. Eq. 40) or only the average cell temperature is desired, the conduction term can be further diminished by integrating boundary conditions into the equation. The resulting time-dependent ordinary differential equation (*i.e.*, Eq. 41) has been widely used in lead-acid,[23-25] nickel-hydrogen,[26,27] lithium-polymer,[28,29] and lithium-ion[30] battery models.

For a thermal model a battery can be thermally and electrochemically coupled or decoupled, depending on how the heat generation term is treated. During battery operation, the heat generation rate depends not only on the cell temperatures but also on charge or discharge regimens. A fully coupled model uses newly produced current and potential information from the model to calculate the heat generation rate and hence temperature distribution, which in turn determines the current and potential,[21,25,27] whereas a decoupled model may employ empirical equations (*e.g.*, the Shepherd equation) describing experimental battery charge/discharge curves of different rates at constant temperature.[18-20,22] The decoupled model is much simpler, but accurate only when battery performance is insensitive to temperature. The complexity of the coupled model can be significantly reduced by the partially coupled approach proposed by Pals and Newman;[7] that is, estimating the heat generation rate during nonisothermal discharge from that obtained at constant temperatures from an isothermal cell model. In other words, heat-generation rates are approximated to be independent of discharge history.

The heat generation rate depends on the thermodynamic properties of the reactions proceeding in a cell, the potential-current characteristics of the cell, and the rates of charge and discharge. By utilizing the first law of thermodynamics for an isobaric battery system, Bernardi *et al.*[31] gave a general energy balance equation for a cell in which the rate of heat generation was given by

$$q = \sum_j I_j\left(U_j^{av} - T\frac{\partial U_j^{av}}{\partial T}\right) - IV + \text{enthalpy-of-mixing term} + \text{phase change term} \qquad [2]$$

where I_j is the volumetric partial reaction current resulting from electrode reaction j, U_j^{av} is the corresponding open-circuit potential (OCP) with superscript av referring to the value evaluated at the average composition, I the total current in the unit of A/cm^3, and V

* Electrochemical Society Student Member.
** Electrochemical Society Active Member.
z E-mail: cxw31@psu.edu

S0013-4651(00)02-015-2 CCC: $7.00

the cell potential. The first term on the right side (RS) of Eq. 2 represents the enthalpy of charge-transfer reactions. The second term stands for the electrical work done by the battery. The third term or the enthalpy-of-mixing term represents the heat effect associated with concentration gradients developed in the cell. The last term or the phase-change term stands for the heat effect due to phase transformations. In arriving at Eq. 2, the energy balance was performed over the entire cell with the assumption of uniform cell temperature. When a cell is thin and the end effects are negligible, the uniformity in temperature is a good approximation. Apparently, when multiple electrode reactions occur simultaneously, the partial current of each reaction must be known in order to calculate the heat generation rate using Eq. 2.

For a battery system that involves an insertion reaction, such as lithium-based and nickel-based batteries, the OCP is a strong function of the local state of charge (SOC), which is often controlled by solid-state species diffusion. During operation at high rates, the species concentration distribution in a cell could be highly nonuniform and result in nonuniform electrochemical reaction rates. Neglecting enthalpy-of-mixing and phase-change terms, Rao and Newman[32] most recently presented a general energy balance equation for insertion battery systems, in which the rate of heat generation is written as

$$q = -\frac{1}{V_c}\int_{V_c}\sum_j a_{sj}\bar{i}_{nj}\left(U_j - T\frac{\partial U_j}{\partial T}\right)dV - IV \qquad [3]$$

where a_{sj} is the specific surface area active for electrode reaction j, $\bar{i}_{nj}$ the transfer current density due to reaction j, and U_j the local OCP of reaction j. A similar expression of the heat generation rate was recently presented by De Vidts *et al.*[27] for a nickel-hydrogen cell, with the pressure work additionally taken into account. Unlike Eq. 2, Eq. 3 relates the heat generation to the local electrochemical reaction rates and the local OCPs and thus is capable of calculating heat generation rate when cells undergo relaxation under dynamic conditions.[32]

It is expected that thermal runaway is first triggered by the hottest spot in a cell. There is thus a need to predict the temperature distribution within a cell in order to capture the thermal runaway process. Based on overall heat balance of a cell, both Eq. 2 and 3 become inadequate when the temperature profile inside a cell is desired.

In the next section, a thermal energy equation capable of describing the internal temperature distribution of the cell is developed based on first principles using the volume-averaging approach. A fully coupled thermal and electrochemical model is then developed by coupling the thermal equation with the previous multiphase transport and electrochemical model.[2] Simplifications to various calculations of the heat generation rate are discussed. The full capability of the model to predict temperature distributions inside cells has been demonstrated elsewhere.[49] In this paper, numerical simulations based on a lumped thermal model are carried out to examine the significance of thermal and electrochemical coupling and to investigate the effects of thermal environment on the electrochemical and thermal behaviors of a Ni-MH (metal hydride) cell under various charging modes.

Model Development

Consider an electrochemical system consisting of porous electrodes, an electrolyte, and a gas phase. The electrolyte can be either liquid or solid. The gas phase is present in batteries due to gas generation accompanying the primary reactions.

General thermal energy equation.—For a multicomponent system such as electrolytic solution, a general differential equation of thermal energy balance has been deduced based on first principles.[33,34] With the assumptions of negligible heat effects due to viscous dissipation and pressure work, no body force, and no homogeneous chemical reactions, this general energy equation is reduced to

$$\rho_k c_{pk}\left(\frac{\partial T_k}{\partial t} + \mathbf{v}_k\cdot\nabla T_k\right) = -\nabla\cdot\mathbf{q}_k + \sum_{\text{species}}\hat{H}_k\nabla\cdot\mathbf{J}_k \qquad [4]$$

where ρ and c_p are the density and specific heat, respectively, T is the temperature, $\mathbf{v}$ is the velocity vector, $\mathbf{q}$ is the heat flux, $\mathbf{J}$ is the molar flux of a species due to diffusion and migration, and $\hat{H}$ is the species partial molar enthalpy, with subscript k denoting in phase k. The second term on the RS of Eq. 4 thus represents thermal transport due to species diffusion and migration, with the summation carried out over all species in phase k.

In general, the heat flux $\mathbf{q}$ includes conductive flux (or Fourier flux), flux caused by interdiffusion of various species, and the Dufour energy flux (or diffusion-thermo effect). Because Dufour energy flux is usually negligible,[33,34] the heat flux $\mathbf{q}$ can be expressed as

$$\mathbf{q}_k = -\lambda_k\nabla T_k + \sum_{\text{species}}\hat{H}_k\mathbf{J}_k \qquad [5]$$

where λ_k is the thermal conductivity of phase k. Applying Eq. 5 and the continuity equation for phase k

$$\nabla\cdot\mathbf{v}_k = 0 \qquad [6]$$

Equation 4 becomes

$$\rho_k c_{pk}\left(\frac{\partial T_k}{\partial t} + \nabla\cdot(\mathbf{v}_k T_k)\right) = \nabla\cdot(\lambda_k\nabla T_k) - \sum_{\text{species}}\mathbf{J}_k\cdot\nabla\hat{H}_k \qquad [7]$$

Use the thermodynamic relationship[34]

$$\hat{H}_k = \mu_k - T\frac{\partial\mu_k}{\partial T} \qquad [8]$$

along with the electrochemical potential defined by[34]

$$\mu_k = \mu_k^o + RT\ln\left(\frac{a_k}{a_{k,ref}}\right) + zF\phi_k \qquad [9]$$

where μ_k^o and a_k are the standard chemical potential and the activity of a species in phase k, respectively, and $a_{k,ref}$ is the species activity at a reference state. One has

$$\nabla\hat{H}_k = -R\nabla\left[T^2\frac{\partial\ln\left(\frac{a_k}{a_{k,ref}}\right)}{\partial T}\right] + zF\nabla\left(\phi_k - T\frac{\partial\phi_k}{\partial T}\right) \qquad [10]$$

Equation 10 holds true with no additional assumptions. The first term on the RS of Eq. 10 is closely related to the enthalpy-of-mixing and has been generally neglected in practice.[27,30,32] Further ignoring the temperature dependence of phase potential for simplicity, Eq. 10 is then simplified to

$$\nabla\hat{H}_k = zF\nabla\phi_k \qquad [11]$$

Substituting Eq. 11 into Eq. 7 yields

$$\rho_k c_{pk}\left(\frac{\partial T_k}{\partial t} + \nabla\cdot(\mathbf{v}_k T_k)\right) = \nabla\cdot\lambda_k\nabla T_k - \sum_{\text{species}}zF\mathbf{J}_k\cdot\nabla\phi_k \qquad [12]$$

Noting that the current through phase k results from diffusion and migration of ionic species in the phase under the assumption of electroneutrality, *i.e.*

$$i_k = \sum_{\text{species}}zF\mathbf{J}_k \qquad [13]$$

Equation 12 can be rewritten as

$$\rho_k c_{pk}\left(\frac{\partial T_k}{\partial t} + \nabla\cdot(\mathbf{v}_k T_k)\right) = \nabla\cdot\lambda_k\nabla T_k - \mathbf{i}_k\cdot\nabla\phi_k \qquad [14]$$

S0013-4651(00)02-015-2 CCC: $7.00

The second term on the RS of Eq. 14 represents the conversion of electrical energy to thermal energy (*i.e.*, Joule heating) and is an important difference between electrical and nonelectrical systems.

Electrochemical reactions occur at the interface between the electrode and the electrolyte. Heat balance over the interface results in[35,36]

$$\lambda_e \nabla T_e \cdot \mathbf{n}_e + \lambda_s \nabla T_s \cdot \mathbf{n}_s = \bar{i}_n \eta + \bar{i}_n \Pi \quad [15]$$

where **n** represents the normal unit vectors pointing outward from a phase, with subscripts e and s denoting the phase of electrolyte and the phase of solid active material, respectively, and $\bar{i}_n$ is the local transfer current density due to the electrode reaction. The RS of Eq. 15 stands for the heat generated at the electrode/electrolyte interface and is divided into two parts. The first term is the irreversible reaction heat due to the electrochemical reaction resistance at the interface, similar to Joule heating. It is proportional to the surface overpotential η of the electrode reaction and is always positive. The second term is the reversible part of the reaction heat mainly due to the entropy change of the electrode reaction. It is called Peltier heat and changes sign with changing current direction. The Peltier coefficient Π can be determined experimentally.[37] It is worth mentioning that in arriving at Eq. 15, the heat effect associated with nonelectrochemical processes, such as water condensation and evaporation occurring in a nickel-hydrogen cell,[26] hydride formation in the MH electrode,[11] and active material decomposition in lithium-ion cells,[30] has not been considered. More generally, Eq. 15 can be rewritten as

$$\lambda_k \nabla T_k \cdot \mathbf{n}_k + \lambda_m \nabla T_m \cdot \mathbf{n}_m = \frac{\sum_j a_{sj} \bar{i}_{nj} (\eta_j + \Pi_j) + (h_k - h_m)\Gamma_{km}}{a_{km}} \quad [16]$$

for the interface at which phase transformation as well as multiple electrochemical reactions take place. Here Γ_{km} represents the phase transformation rate at the k-m interface from phase m to phase k, a_{sj} is the specific surface area active for electrode reaction j, $a_{km} = A_{km}/V_o$ is the specific surface area of the k-m interface within the averaging volume V_o, and h is the enthalpy with subscripts k and m referring to phases k and m, respectively. On the RS of Eq. 16, the second term accounts for the heat effect due to the phase transformation taking place at the interface, whereas the first term includes the heat effect due to the electrochemical reactions. For interfaces at which no electrochemical reactions occur, such as gas-involved interfaces, the first term on the RS simply vanishes.

Let V_o be the volume of an REV consisting of V_k (k = e, s, and g for electrolyte, solid active material, and gas phases, respectively) and follow the procedures described in Ref. 1. Volume-averaging of Eq. 14 over the REV yields

$$\rho_k c_{pk} \left[\frac{\partial \epsilon_k <T_k>^k}{\partial t} + \nabla \cdot \left(\epsilon_k <T_k>^k <\mathbf{v}_k>^k \right) \right] = \nabla \cdot \left[\left(\lambda_k^{eff} + \lambda_{a,k} \right) \nabla <T_k>^k \right] + \sum_m \left(Q_{km}^d + Q_{km}^\Gamma \right) - <\mathbf{i}_k> \cdot \nabla <\phi_k>^k + Q_k^{Joule} \quad [17]$$

with

$$Q_{km}^d = \frac{1}{V_o} \int_{A_{km}} \lambda_k \nabla T_k \cdot \mathbf{n}_k dA \quad [18]$$

$$Q_{km}^\Gamma = \frac{1}{V_o} \int_{A_{km}} \rho_k c_{pk} T_k (\mathbf{w}_k - \mathbf{v}_k) \cdot \mathbf{n}_k dA \quad [19]$$

and

$$Q_k^{Joule} = -<\mathbf{i}_k>^k \cdot \frac{1}{V_o} \int_{A_{km}} \left(\phi_k - <\phi_k>^k \right) \mathbf{n}_k dA - \frac{1}{V_o} \int_{V_k} \left(\mathbf{i}_k - <\mathbf{i}_k>^k \right) \cdot \nabla \left(\phi_k - <\phi_k>^k \right) dV \quad [20]$$

where λ_k^{eff} is the effective thermal conductivity of phase k and $\lambda_{a,k}$ is the dispersion coefficient in phase k. While λ_k^{eff} includes the effect of tortuosity and may follow the Bruggeman correction (*i.e.*, $\lambda_k^{eff} = \epsilon_k^{1.5} \lambda_k$), $\lambda_{a,k}$ represents the effect of hydrodynamic dispersion that results from variations of the microscopic velocity and temperature and vanishes in the absence of fluid motion.

The second term on the RS of Eq. 17 is the sum of interfacial heat-transfer effects. Q_{km}^d represents the interfacial heat-transfer rate due to conduction, whereas Q_{km}^Γ stands for the thermal effect due to the interface movement at a velocity of $\mathbf{w}_k$. In view of the mean values for integrals, Q_{km}^Γ can be modeled as the product of the average interfacial temperature by the phase transformation rate at the interface, *i.e.*

$$Q_{km}^\Gamma = c_{pk} \bar{T}_{km} \Gamma_{km} \quad [21]$$

where $\bar{T}_{km}$ is the area-averaged temperature at the k-m interface.

The last term on the RS of Eq. 17, Q_k^{Joule}, arises from volume-averaging the Joule heating term in Eq. 14. Apparently, it would vanish when electrical equilibrium holds true in a phase, *i.e.*, $\phi_k = <\phi_k>^k$. However, electrical nonequilibrium is expected if the phase conductivity is low and/or the applied current density is high.[1] The conductivity of semiconductor-like active materials (*e.g.*, NiOOH) can be as low as 10^{-5} S/cm. Such a low electronic conductivity may cause a significant microscopic ohmic drop across the active material layer coated on a substrate.[1] In this case, it can be shown that the first term on the RS of Eq. 20 is still negligible (see the Appendix). However, the magnitude of the second term cannot be easily estimated and, thus, it is left unmodeled in the present work. Physically, this term arises from fluctuations in the profiles of microscopic current and potential. Quantification of this term will be attempted in future work.

Summation of Eq. 17 over all phases involved in the REV (*i.e.*, the electrolyte phase, the solid active material phase, and the gas phase) and use of Eq. 18 yield

$$\sum_k \left\{ \rho_k c_{pk} \left[\frac{\partial \epsilon_k <T_k>^k}{\partial t} + \nabla \cdot \left(\epsilon_k <T_k>^k <\mathbf{v}_k>^k \right) \right] \right\} = \sum_k \left\{ \nabla \cdot \left[\left(\lambda_k^{eff} + \lambda_{a,k} \right) \nabla <T_k>^k \right] \right\} = \sum_{k \neq m} \sum_m \left(\frac{1}{V_o} \int_{A_{km}} \lambda_k \nabla T_k \cdot \mathbf{n}_k dA + c_{pk} \bar{T}_{km} \Gamma_{km} \right) - \sum_k \left(<\mathbf{i}_k> \cdot \nabla <\phi_k>^k \right) \quad [22]$$

Applying Eq. 16, Eq. 22 becomes

$$\sum_k \left\{ \rho_k c_{pk} \left[\frac{\partial \epsilon_k <T_k>^k}{\partial t} + \nabla \cdot \left(\epsilon_k <T_k>^k <\mathbf{v}_k>^k \right) \right] \right\} = \sum_k \left[\nabla \cdot \left(\lambda_k^{eff} \nabla <T_k>^k \right) \right] + \sum_j a_{sj} \bar{i}_{nj} \left(\bar{\eta}_j + \Pi_j \right) = \sum_{k \neq m} \sum_m \left[(h_k - h_m)\Gamma_{km} + (c_{pk} - c_{pm}) \bar{T}_{km} \Gamma_{km} \right] - \sum_k \left(<\mathbf{i}_k> \cdot \nabla <\phi_k>^k \right) \quad [23]$$

S0013-4651(00)02-015-2 CCC: $7.00

Assuming that local thermal equilibrium exists in the system under consideration, *i.e.*

$$<T_k>^k = <T_m>^m = \overline{T}_{km} = \overline{T}_{mk} = T \quad [24]$$

and dropping the volume-averaged symbols for convenience, Eq. 23 becomes

$$\frac{\partial\left(\rho c_p T\right)}{\partial t} + \nabla\cdot(\mathbf{v}T) = \nabla\cdot\lambda\nabla T + q \quad [25]$$

where

$$\rho c_p = \sum_k \epsilon_k \rho_k c_{pk} \quad [26]$$

$$\mathbf{v} = \sum_k \epsilon_k \rho_k c_{pk} <\mathbf{v}_k>^k \quad [27]$$

$$\lambda = \sum_k \left(\lambda_k^{eff} + \lambda_{a,k}\right) \quad [28]$$

and the heat-source term, q, is given by

$$q = \sum_j a_{sj}\bar{i}_{nj}\left(\overline{\eta}_j + \Pi_j\right) + \sum_{k\neq m}\sum_m \left(\Delta h^* \Gamma_{km}\right) - \sum_{k=e\&s}\left(<\mathbf{i}_k>\cdot\nabla<\phi_k>^k\right) \quad [29]$$

with

$$\Delta h^* = (h_k - h_m) + (c_{pk} - c_{pm})T \quad [30]$$

The volume-averaged current density through phase k takes the form of [1]

$$<\mathbf{i}_k> = -\kappa^{eff}\nabla<\phi_e>^e - \kappa_D^{eff}\nabla \ln <c_e^i> \quad i = + \text{ or } - \quad [31]$$

for the phase of a concentrated binary electrolyte, and

$$<\mathbf{i}_s> = -\sigma^{eff}\nabla<\phi_s>^s \quad [32]$$

for the phase of a solid active material, where κ is the ionic conductivity of the electrolyte, κ_D is the diffusional conductivity, and σ is the solid electronic conductivity, with superscript eff indicating the effects of porosity and tortuosity included. Note that there is no current flowing through the gaseous phase.

Equation 29 shows that the thermal effects are due to electrochemical reactions, phase transformation, and ohmic Joule heating in both the electrolyte and solid active material phases. Because the reaction heat is expressed in terms of the local transfer current density, the heat effect resulting from a highly nonuniform distribution in the reaction rate can be assessed. Equation 25 enables one to determine temperature distributions inside a cell rather than to obtain only an average temperature of the cell.

In order to calculate the heat generation rate using Eq. 29, the Peltier coefficient, Π_j, must be known. An expression for Peltier coefficient has been derived by Newman[35] based on the general multicomponent transport equations and electrode reactions. With the Dufour energy flux neglected, it is reduced to

$$\Pi_j = \frac{T\Delta S_j}{n_j F} \quad [33]$$

where ΔS_j is the entropy change of electrode reaction j. Entropy changes of a number of electrode reactions were calculated by Lampinen and Fomino[38] and by Xu *et al.*[39]

Alternatively, using the following thermodynamic relationship between the OCP U_j and the entropy change ΔS_j [40]

$$\Delta S_j = n_j F \frac{\partial U_j}{\partial T} \quad [34]$$

the Peltier coefficient can be rewritten as

$$\Pi_j = T\frac{\partial U_j}{\partial T} \quad [35]$$

Substituting Eq. 35 and $\overline{\eta}_j = \overline{\phi}_{se} - \overline{\phi}_{es} - U_j$ into Eq. 29 gives

$$q = -\sum_j a_{sj}\bar{i}_{nj}\left(U_j - T\frac{\partial U_j}{\partial T}\right) + \sum_j a_{sj}\bar{i}_{nj}\left(\overline{\phi}_{se} - \overline{\phi}_{es}\right) + \sum_{k\neq m}\sum_m \left(\Delta h^* \Gamma_{km}\right) - \sum_{k=e\&s}\left(<\mathbf{i}_k>\cdot\nabla<\phi_k>^k\right) \quad [36]$$

Equation 25, along with the expression for the heat generation rate, Eq. 36, constitutes a general thermal model that describes the temperature field inside a cell.

Thermal and electrochemical coupling.—Temperature-dependent physicochemical properties, such as the diffusion coefficient and ionic conductivity of the electrolyte, are needed to couple the thermal model with the multiphase mass-transport and electrochemical kinetic model. More specifically, the dependence of the physicochemical properties on the temperature can be described by Arrhenius' equation[21,25,36]

$$\Phi = \Phi_{ref}\ \exp\left[\frac{E_{act,\Phi}}{R}\left(\frac{1}{T_{ref}} - \frac{1}{T}\right)\right] \quad [37]$$

where Φ is a general variable representing the diffusion coefficient of a species, conductivity of the electrolyte, exchange current density of an electrode reaction, etc., with subscript ref denoting the value at a reference temperature. $E_{act,\Phi}$ is the activation energy of the evolution process of Φ. Its magnitude determines the relative sensitivity of the cell to temperature. The greater its activation energy, the more sensitive is the parameter to temperature. The ionic conductivity and electrolyte diffusion coefficient usually are strong functions of the temperature; such data are available for Ni-MH[41] and Li-based[7] batteries.

In addition, the OCP of electrode reaction j, U_j, is usually approximated as a linear function of temperature

$$U_j = U_{j,ref} + \left(T - T_{ref}\right)\frac{\partial U_j}{\partial T} \quad [38]$$

The heat generation rate due to electrochemical reactions and Joule heating are calculated locally via a detailed electrochemical model, and subsequently are used in the energy conservation equation to calculate the temperature evolution. This temperature information is, in turn, fed back to update the electrochemical calculations through temperature-dependent physicochemical properties. Figure 1 shows a schematic diagram of the present coupled modeling approach.

Lumped thermal model.—For most battery systems, the convection term in Eq. 25 can generally be neglected, and a transient heat conduction equation is sufficient to describe thermal phenomena in batteries, *i.e.*

$$\frac{\partial(\rho c_p T)}{\partial t} = \nabla\cdot(\lambda\nabla T) + q \quad [39]$$

Here, the thermal conductivity λ is highly anisotropic and microstructure-dependent because a battery cell is composed of a variety of complex materials.

For single cells of small thickness, one may have

$$Bi = \frac{hL}{\lambda} << 1 \quad [40]$$

S0013-4651(00)02-015-2 CCC: $7.00

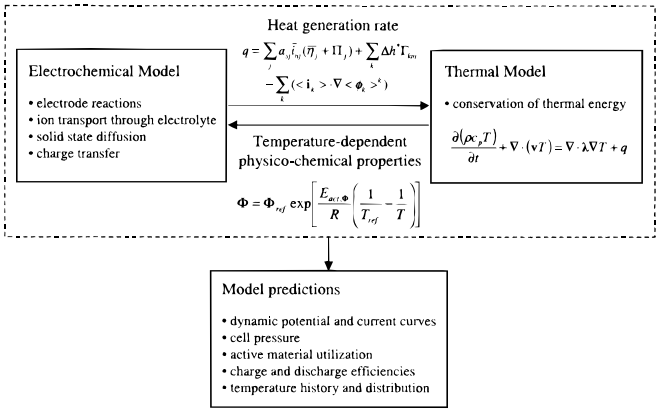

Figure 1. Diagram of the thermal-electrochemical coupled modeling approach.

where h is the convective heat-transfer coefficient, and L and λ are the thickness and the thermal conductivity of the cell, respectively. Under the condition given by Eq. 40, the assumption of a uniform temperature across the cell is valid and hence a lump-parameter model of energy balance can be applied. Equation 39 is thus reduced to

$$\frac{d(\rho c_p T)}{dt} + Q = \frac{1}{V_c}\int_{V_c} q dv = \langle q \rangle \qquad [41]$$

where the heat removal rate per unit volume from the cell to the surroundings, Q, can be expressed using an equivalent convective heat transfer coefficient, h, as follows

$$Q = \frac{hA_c(T - T_a)}{V_c} \qquad [42]$$

where V_c is the cell volume, A_c the surface area through which heat is removed from the cell, and T_a the temperature of surroundings. $\langle q \rangle$ is the volume-averaged heat generation rate in the form of

$$\langle q \rangle = -\frac{1}{V_c}\int_{V_c}\sum_j a_{sj}\bar{i}_{nj}\left(U_j - T\frac{\partial U_j}{\partial T}\right)dv + \frac{1}{V_c}\int_{V_c}\sum_j a_{sj}\bar{i}_{nj}\left(\bar{\phi}_{se} - \bar{\phi}_{es}\right)dv + \frac{1}{V_c}\int_{V_c}\sum_{k\neq m}\sum_m \left(\Delta h^* \Gamma_{km}\right)dv - \frac{1}{V_c}\int_{V_c}\sum_{k=e\&s}\left(\langle \mathbf{i}_k \rangle \cdot \nabla \langle \phi_k \rangle^k\right)dv \qquad [43]$$

We rewrite the second integral of Eq. 43 to obtain

$$\langle q \rangle = -\frac{1}{V_c}\int_{V_c}\sum_j a_{sj}\bar{i}_{nj}\left(U_j - T\frac{\partial U_j}{\partial T}\right)dv + \frac{1}{V_c}\int_{V_c}\sum_j a_{sj}\bar{i}_{nj}\left(\langle \phi_s \rangle^s - \langle \phi_e \rangle^e\right)dv + \frac{1}{V_c}\int_{V_c}\sum_j a_{sj}\bar{i}_{nj}\left[\left(\bar{\phi}_{se} - \langle \phi_s \rangle^s\right) - \left(\bar{\phi}_{es} - \langle \phi_e \rangle^e\right)\right]dv + \frac{1}{V_c}\int_{V_c}\sum_{k\neq m}\sum_m \left(\Delta h^* \Gamma_{km}\right)dv - \frac{1}{V_c}\int_{V_c}\sum_{k=e\&s}\left(\langle \mathbf{i}_k \rangle \cdot \nabla \langle \phi_k \rangle^k\right)dv \qquad [44]$$

The third term on the RS of Eq. 44 results from the electrical nonequilibrium that exists in the solid active material and electrolyte phases. Assuming that the heat effect due to the electrical nonequilibrium is negligible, Eq. 44 then becomes

$$\langle q \rangle = -\frac{1}{V_c}\int_{V_c}\sum_j a_{sj}\bar{i}_{nj}\left(U_j - T\frac{\partial U_j}{\partial T}\right)dv + \frac{1}{V_c}\int_{V_c}\sum_j a_{sj}\bar{i}_{nj}\left(\langle \phi_s \rangle^s - \langle \phi_e \rangle^e\right)dv + \frac{1}{V_c}\int_{V_c}\sum_{k\neq m}\sum_m \left(\Delta h^* \Gamma_{km}\right)dv - \frac{1}{V_c}\int_{V_c}\sum_{k=e\&s}\left(\langle \mathbf{i}_k \rangle \cdot \nabla \langle \phi_k \rangle^k\right)dv \qquad [45]$$

We assume one-dimensional electrochemical processes across the cell thickness, which is generally the case because of the high electronic conductivity of the current collectors bound to the electrodes. Conservation of charge in both solid and electrolyte phases requires[1]

$$\nabla \cdot \langle \mathbf{i}_e \rangle = -\nabla \cdot \langle \mathbf{i}_s \rangle = \sum_j a_{sj}\bar{i}_{nj} \qquad [46]$$

Applying Eq. 46 to the second integral in Eq. 45 and integrating it by parts yield

$$\text{2nd integral in Eq. 45} = -\frac{1}{V_c}\int_{V_c}\nabla \cdot \langle \mathbf{i}_e \rangle \langle \phi_e \rangle^e dv - \frac{1}{V_c}\int_{V_c}\nabla \cdot \langle \mathbf{i}_s \rangle \langle \phi_s \rangle^s dv = -IV + \frac{1}{V_c}\int_{V_c}\sum_{k=e\&s}\left(\langle \mathbf{i}_k \rangle \cdot \nabla \langle \phi_k \rangle^k\right)dv \qquad [47]$$

where $I = iA/V_c = i/L$ is the total volumetric current density (A/cm^3) applied to the cell, with A and L denoting the projected electrode area and the cell width, respectively. To obtain Eq. 47, the following boundary conditions were used

$$\langle \mathbf{i}_e \rangle = 0 \quad \text{at } x = 0 \text{ and } L \qquad [48]$$

$$\langle \mathbf{i}_s \rangle = i \quad \text{at } x = 0 \text{ and } L \qquad [49]$$

with the definition of cell potential

$$V = \langle \phi_s \rangle^s_{|x=L} - \langle \phi_s \rangle^s_{|x=0} \qquad [50]$$

Substituting Eq. 47 into Eq. 45, one has

$$\langle q \rangle = -\frac{1}{V_c}\int_{V_c}\sum_j a_{sj}\bar{i}_{nj}\left(U_j - T\frac{\partial U_j}{\partial T}\right)dv - IV + \frac{1}{V_c}\int_{V_c}\sum_{k\neq m}\sum_m \left(\Delta h^* \Gamma_{km}\right)dv \qquad [51]$$

When the heat effect due to phase transformation is ignored, Eq. 51 is simplified to Eq. 3 presented by Rao and Newman[32] for insertion battery systems.

Two conditions can be applied to further simplify Eq. 51: (*i*) the OCP term, as shown in the parenthesis in Eq. 51, is constant; and (*ii*) the electrode reaction rates are spatially uniform. In the case of constant OCPs, Eq. 51 can be reduced to the following by taking the OCP term out of the integrand

$$\langle q \rangle = \sum_j I_j\left(U_j - \frac{\partial U_j}{\partial T}\right) - IV \qquad [52]$$

where

$$I_j = \frac{1}{V_c}\int_{V_c} a_{sj}\bar{i}_{nj} dv \qquad [53]$$

S0013-4651(00)02-015-2 CCC: $7.00

In the case of uniform reaction rates, the heat generation rate can be rewritten as

$$<q> = \sum_j I_j \left[\frac{1}{V_c} \int_{V_c} \left(U_j - T \frac{\partial U_j}{\partial T} \right) dv \right] - IV$$

$$= \sum_j I_j \left(U_j - T \frac{\partial U_j}{\partial T} \right)_{av} - IV \quad [54]$$

Equation 52 or 54 is identical to Eq. 2 presented by Bernardi *et al.*[31] with neglect of enthalpy-of-mixing and phase-change terms. If only one overall cell reaction (*i.e.,* one pair of electrode reactions) must be considered, Eq. 52 or 54 can be rewritten as

$$<q> = I \left(U - T \frac{\partial U}{\partial T} \right) - IV = I \left(U - V - T \frac{\partial U}{\partial T} \right)$$

$$= \frac{i}{L} \left(U - V - T \frac{\partial U}{\partial T} \right) \quad [55]$$

where U is the open-circuit cell potential determined by the difference between positive and negative electrode OCPs. Equation 55 has been widely used in lead-acid,[23,24] lithium-polymer,[7,18-20,28,29] and lithium-ion[22] battery thermal models. It is clearly shown by the simplifications made that Eq. 55 is accurate only for the overall thermal balance of a cell with no significant heat effect due to phase change, no concentration gradients present in the cell, constant OCPs or uniform reaction rates, and a single overall reaction contributing to reaction heat. Rao and Newman[32] have illustrated that significant errors may occur when Eq. 55 is used to calculate the heat generation rate instead of Eq. 3. The extent of error depends greatly on the temporal behavior of the electrode OCP. Equation 55 virtually fails for a dynamic discharge in which cell relaxation is involved.[32]

Application to Ni-MH Cells

A thermal and electrochemical coupled model results by combining the thermal equation derived previously with the micro-macroscopic multiphase transport and electrochemical model previously developed for Ni-MH cells.[2] The model not only accounts for the microscopic diffusion of proton and hydrogen in solid active materials, but also incorporates oxygen reactions and transport through both electrolyte and gas phases. Model details have been presented in Ref. 2 and hence are not repeated here. Equation 41, *i.e.,* the lumped-parameter thermal equation, is employed in the following simulations as a first step. Applying Eq. 51 to a Ni-MH cell, one has

$$<q> = -\frac{1}{V_c} \int_{V_c} \sum_j a_{sj} \bar{i}_{nj} \left(U_j - T \frac{\partial U_j}{\partial T} \right) dv - IV$$

$$+ \frac{1}{V_c} \int_{V_c} \left(\Delta h^*_{hyd} a_{s3} \bar{i}_{n3} \right) dv \quad [56]$$

where Δh^*_{hyd} is the enthalpy of metal hydride formation. Equation 56 is used to calculate the volume-averaged heat generation rate of the Ni-MH cell. The model equations are summarized in Table I, subject to the following initial and boundary conditions.

Initial conditions.—Species concentrations are uniform at time = 0, *i.e.*

$$c^{OH} = c^{OH}_o, \; c^{O_2}_e = c^{O_2}_{e,o}, \; c^{O_2}_g = c^{O_2}_{g,o}, \; c^{H} = c^{H}_o, \quad \text{and} \quad T = T_o \quad [57]$$

Table I. Summary of model equations for a Ni-MH battery.

Species concentration in liquid phase	$\frac{\partial(\epsilon_e c^{OH})}{\partial t} = \nabla \cdot \left(D^{OH}_{eff} \nabla c^{OH} \right) + \frac{t^o_- - 1}{F} j^{OH}$
	$\frac{\partial(\epsilon_e c^{O_2}_e)}{\partial t} = \nabla \cdot \left(D^{O_2}_{e,eff} \nabla c^{O_2}_e \right) + \frac{1}{4F} j^{O_2} + J^{O_2}_{eg}$
Species concentration in gas phase	$\frac{\partial c^{O_2}_g}{\partial t} = -\frac{1}{V_g} \int_V J^{O_2}_{eg} dv$
Species concentration in solid phase	$\frac{\partial(\epsilon_s c^{H})}{\partial t} = \frac{j^{H}}{F}$
	$\frac{D^{H}}{l_{se}} \left(\bar{c}^{H}_{se} - c^{H} \right) = \frac{j^{H}}{a_{se} F}$
Liquid phase potential	$\nabla \cdot \left(\kappa^{eff} \nabla \phi_e \right) + \nabla \cdot \left(\kappa^{eff}_D \nabla \ln c^{OH} \right) + j^{OH} = 0$
Solid phase potential	$\nabla \cdot \left(\sigma^{eff} \nabla \phi_s \right) - j^{OH} + a_{sb} \frac{\bar{\phi}_{sb} - \phi_s}{R_{sb}} = 0$
	$\frac{\bar{\phi}_{se} - \phi_s}{R_{se}} = -\frac{j^{OH}}{a_{se}}$
Cell temperature	$\frac{d(\rho c_p T)}{dt} = <q> + \frac{h A_c (T - T_a)}{V_c}$
	$<q> = -\frac{1}{V_c} \int_{V_c} \sum_j a_{sj} \bar{i}_{nj} \left(U_j - T \frac{\partial U_j}{\partial T} \right) dv - IV + \frac{1}{V_c} \int_{V_c} \left(\Delta h^*_{hyd} a_{s3} \bar{i}_{n3} \right) dv$

S0013-4651(00)02-015-2 CCC: $7.00

Boundary conditions.—There is no flux of species and all current goes through the solid, therefore

$$\frac{\partial c^{OH}}{\partial x} = 0, \quad \frac{\partial c_e^{O_2}}{\partial x} = 0, \quad \text{and} \quad \frac{\partial \phi_e}{\partial x} = 0$$

at the electrode/current collector interfaces [58]

The boundary conditions for solid-phase potential are dependent on the operation mode. At the positive electrode/current collector interface ($x = L$)

$$\phi_s = 0 \text{ (reference potential)} \quad [59]$$

At the negative electrode/current collector interface ($x = 0$)

$$\begin{aligned} \phi_s &= -V \qquad \text{for floating charge} \\ -\sigma^{eff}\frac{\partial \phi_s}{\partial x} &= i \qquad \text{for galvanic charge} \end{aligned} \quad [60]$$

where V and i are applied voltage and current density, respectively.

Cell 2 in the previous work[2] is used to investigate the electrochemical and thermal behaviors of a Ni-MH cell under various operation modes and thermal conditions. Its cell-specific parameters have been given therein.[2] The operation modes include constant current charging at the 1C rate (*i.e.*, $i = 35.7$ mA/cm^2) and float charging at a constant cell voltage of 1.5 V. Four thermal conditions are considered in terms of an equivalent heat-transfer coefficient imposed on the cooling surface of the cell. Whereas h = 0 and ∞ correspond to adiabatic and isothermal conditions, respectively, h = 5 and 25 W/m^2 K refer to typical values of air-free convection and forced convection (*e.g.*, via a cooling fan). In other words, active thermal management is necessary in order to achieve a convective heat-transfer coefficient of 25 W/m^2 K. Table II lists the values of parameters used in the thermal modeling of the Ni-MH battery. Other values of parameters needed in the simulations can be found in Ref. 2.

The partial heat generation rates to be discussed in the next section are defined as

$$\langle q\rangle^{P} = -\frac{1}{L}\int_0^L \sum_j a_{sj}\bar{i}_{nj}\left(\langle\phi_s\rangle^{s} - \langle\phi_e\rangle^{e} - \left(U_j - T\frac{\partial U_j}{\partial T}\right)\right)dx$$

j = 1 and 3 [61]

$$\langle q\rangle^{O} = -\frac{1}{L}\int_0^L \sum_j a_{sj}\bar{i}_{nj}\left(\langle\phi_s\rangle^{s} - \langle\phi_e\rangle^{e} - \left(U_{O_2} - T\frac{\partial U_{O_2}}{\partial T}\right)\right)dx$$

j = 2 and 4 [62]

$$\langle q\rangle^{H} = -\frac{1}{L_{MH}}\int_0^{L_{MH}}\left(\Delta h^*_{hyd} a_{s3}\bar{i}_{n3}\right)dx \quad [63]$$

and

$$\langle q\rangle^{J} = -\frac{1}{L}\int_0^L \sum_{k=e\&s}\left(\langle \mathbf{i}_k\rangle\cdot\nabla\langle\phi_k\rangle^{k}\right)dx \quad [64]$$

where the superscripts P, O, H, and J denote the partial heat generation rates due to the primary reactions 1 and 3, oxygen reactions 2 and 4, hydride formation, and Joule heating, respectively. L_{MH} is the thickness of the metal hydride electrode.

The partial currents presented in the Results and Discussion section are defined as

$$i_P = \int_{L-L_{Ni}}^{L} a_{s1}\bar{i}_{n1}dx \quad [65]$$

and

$$i_{O_2} = \int_{L-L_{Ni}}^{L} a_{s2}\bar{i}_{n2}dx \quad [66]$$

where i_P and i_{O_2} represent the partial currents due to the primary reaction 1 and oxygen generation reaction 2 in the nickel electrode, respectively. L_{Ni} is the thickness of the nickel electrode.

Table II. Values of parameters used in the thermal modeling of a Ni-MH battery.

Symbol	Value	Unit	Description
ρ_e	1.25	g/cm^3	Density of KOH electrolyte[41]
ρ_{Ni}	3.55	g/cm^3	Density of nickel electrode[42]
ρ_{MH}	7.49	g/cm^3	Density of MH electrode[42]
ρ_{sep}	0.9	g/cm^3	Density of polyamide separator[a]
$c_{p,e}$	3.2	J/g K	Specific heat of KOH electrolyte[41]
$c_{p,Ni}$	0.88	J/g K	Specific heat of nickel electrode[41]
$c_{p,MH}$	0.35	J/g K	Specific heat of MH electrode[43]
$c_{p,sep}$	1.9	J/g K	Specific heat of polyamide separator[41]
$(dU/dT)_{ref}$	−1.125	mV/K	Temperature coefficient of reference electrode OCP[44]
$(dU/dT)_{Ni}$	−1.35	mV/K	Temperature coefficient of nickel electrode OCP[44]
$(dU/dT)_{MH}$	−0.836	mV/K	Temperature coefficient of MH electrode OCP[44 b]
$(dU/dT)_{O_2}$	−1.68	mV/K	Temperature coefficient of oxygen reaction OCP[44]
Δh^*_{hyd}	−30.4	kJ/mol H_2	Enthalpy of metal hydride ($LaNi_5H_6$) formation[41,43]
$E_{act,Ni}$	20	kJ/mol	Activation energy of nickel electrode reaction[45]
$E_{act,MH}$	30	kJ/mol	Activation energy of MH electrode reaction[4]
E_{act,O_2}	50	kJ/mol	Activation energy of oxygen reaction [45]
$E_{act,D^{OH}}$	14	kJ/mol	Activation energy of electrolyte diffusion[46]
$E_{act,D^{O_2}}$	14	kJ/mol	Activation energy of oxygen diffusion in KOH electrolyte[47]
$E_{act,D^{H^+}}$	9.62	kJ/mol	Activation energy of proton diffusion in nickel active material[48]
$E_{act,D^{H}}$	10	kJ/mol	Activation energy of atomic hydrogen diffusion in MH particles[a]
$E_{act,\kappa}$	13	kJ/mol	Activation energy of electrolyte conductivity[41 c]

[a] Estimated value.
[b] Take the data of $H_2O(l)/H_2(g)$, OH^- electrode.
[c] Evaluated using the data in Fig. 5 of Ref. 41.

S0013-4651(00)02-015-2 CCC: $7.00

Results and Discussion

Significance of thermal-electrochemical coupling.—The need for a thermal-electrochemical coupled model can be demonstrated clearly by comparisons of predicted cell potential, pressure, and temperature using the coupled and decoupled models, respectively. The decoupled model assumes that the electrochemical submodel is essentially temperature-independent. However, because temperature is included in the Butler-Volmer equation, the decoupled model results are still dependent on the thermal history and thus on the heat-transfer coefficient. Figure 2 displays comparisons of predicted cell potential curves during 1C charging. An apparent discrepancy between the coupled and decoupled model predictions begins from 10% charge input and becomes significant when approaching the overcharge region. The discrepancy decreases with increasing heat-transfer coefficient, because a higher heat-transfer coefficient yields a larger heat dissipation rate and hence a smaller temperature rise during battery charging. As expected, the decoupled model is applicable only when the variation in cell temperature is sufficiently small.

Unlike the cell potential, the cell temperature and pressure are insensitive to the thermal-electrochemical coupling during constant-current charging, as shown in Fig. 3. It also shows that the cell temperature decreases significantly with increasing heat-transfer coefficient, while the reduction in cell pressure is very small.

Figure 4 plots the current density applied to the cell during float charging at a voltage of 1.5 V. A significant discrepancy is observed between the coupled and decoupled model predictions when the heat dissipation is poor (corresponding to a small heat-transfer coefficient). The discrepancy becomes smaller when a higher heat-transfer coefficient is applied. This, again, indicates that the decoupled model is valid only when the variation in the cell temperature is insignificant.

Figure 5 shows the comparisons of predicted cell pressure and temperature during the float charging. The decoupled model significantly underpredicts the cell pressure and temperature under poorer heat dissipation conditions. A thermal-electrochemical coupled model is necessary in order to accurately predict pressure buildup in a Ni-MH battery and ensure its safe operation. In view of the inaccuracy of the decoupled approach, the coupled model is used to perform all following numerical studies.

Thermal effects during constant-current charging.—Figure 6 shows electrochemical and thermal behaviors of the Ni-MH cell during 1C charging. As the heat-transfer coefficient decreases, the cell potential increases more slowly and the potential peak becomes more pronounced. The cell temperature increases with time in all cases, indicating that the cell is exothermic when charged at 1C. A larger heat-transfer coefficient corresponds to a larger rate of heat dissipation, resulting in a smaller temperature rise. When the heat-transfer coefficient is larger than 5 W/m^2 K, the cell temperature rise is less than 5°C when the charge input is less than 90% of the nominal cell capacity. After that stage, the cell temperature increases dra-

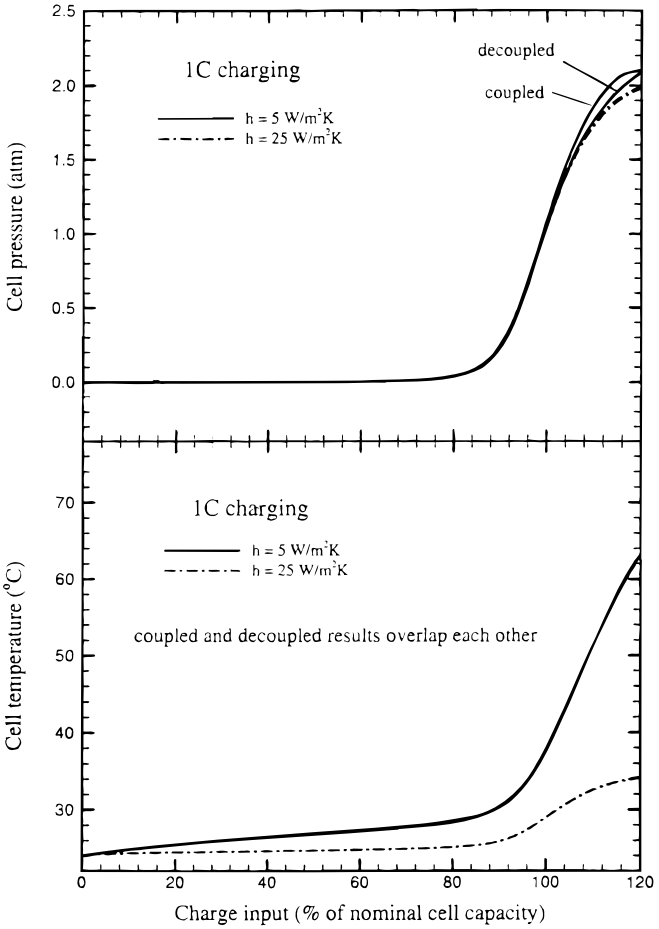

Figure 3. Comparisons of predicted cell temperature and pressure evolutions between the coupled and decoupled thermal-electrochemical models during 1C charging.

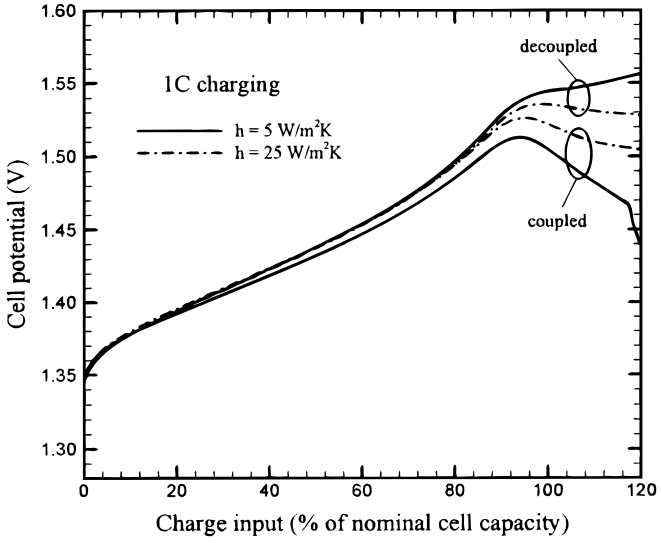

Figure 2. Comparisons of predicted potential curves between the coupled and decoupled thermal-electrochemical models during 1C charging.

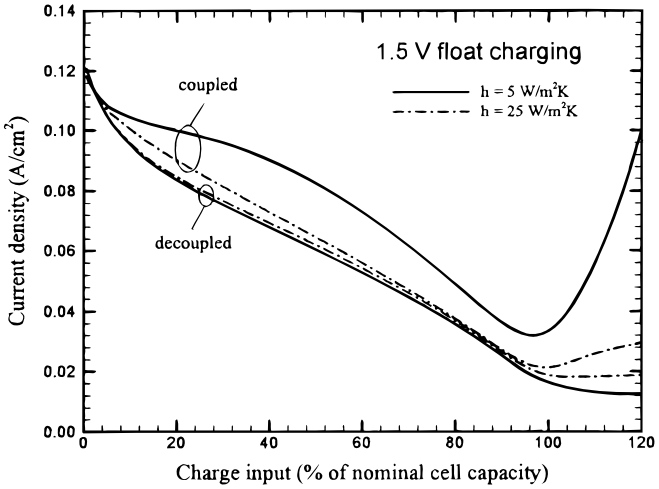

Figure 4. Comparisons of predicted current density variations between the coupled and decoupled thermal-electrochemical models during 1.5 V charging.

S0013-4651(00)02-015-2 CCC: $7.00

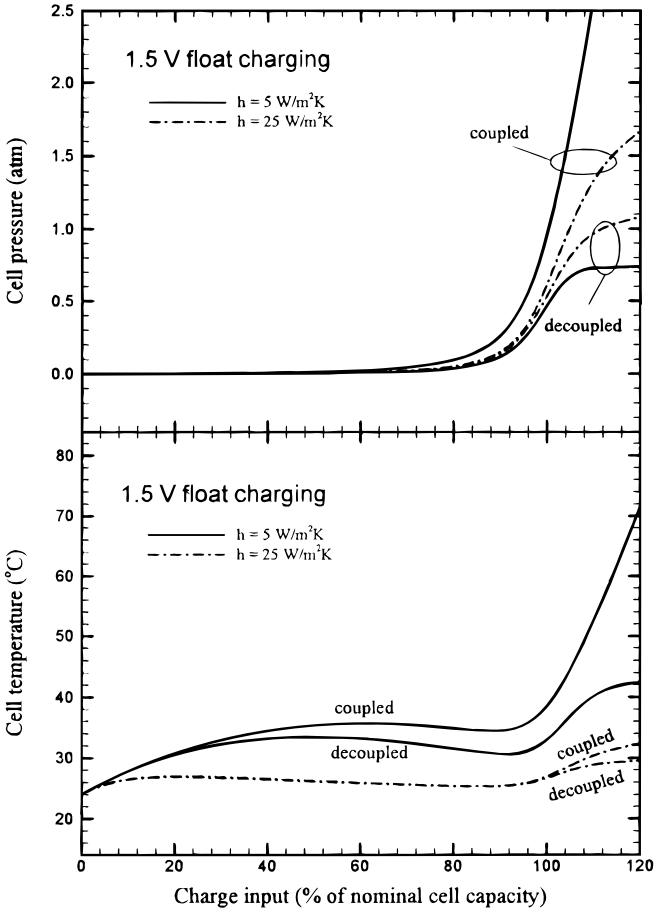

Figure 5. Comparisons of predicted cell temperature and pressure evolutions between the coupled and decoupled thermal-electrochemical models during 1.5 V float charging.

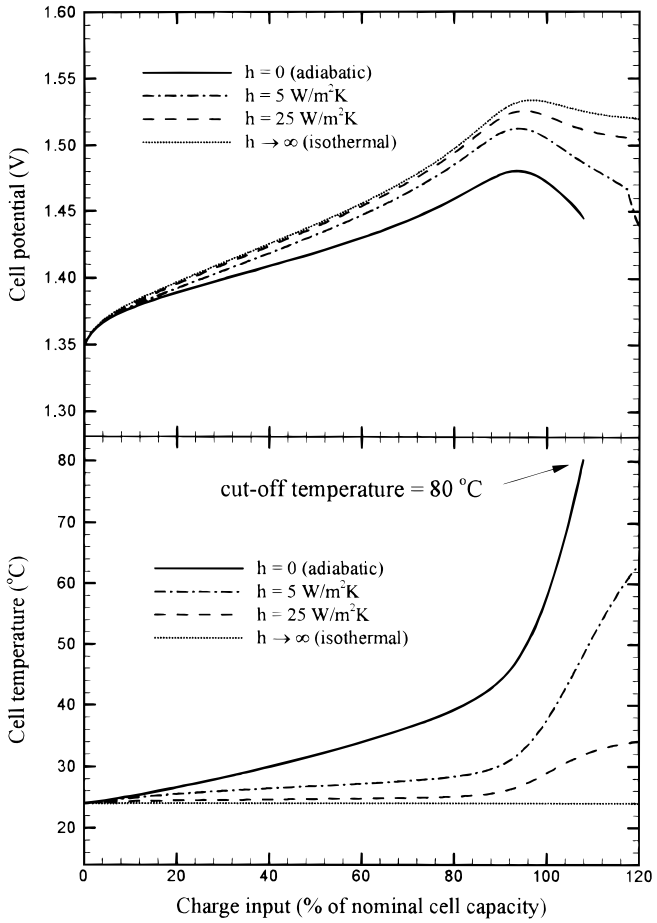

Figure 6. Cell potential and temperature evolutions during 1C charging under various thermal conditions.

matically up to 64°C at 120% charge input when the heat-transfer coefficient equals 5 W/m^2 K. As the heat-transfer coefficient increases, the final cell temperature decreases. A less than 10°C increase from the original temperature is observed when the heat-transfer coefficient is as large as 25 W/m^2 K. The cell temperature exceeds the safety limit for an aqueous cell (80°C) when the cell is charged in an adiabatic condition, showing the need for thermal management for Ni-MH batteries.

The overall trend in the cell temperature during 1C charging can be explained using Fig. 7, which plots the total and partial heat generation rates of the cell *vs.* charge input. The total heat generation rate increases slowly before 90% charge input, jumps quickly thereafter, and finally reaches a steady state, closely matching the trend in temperature variation. Surprisingly, the thermal environmental condition has little effect on the heat generation rate. Because the overall reaction current is fixed when a battery is charged at a constant current, slight variations in the total heat generation rate results only from the difference in the ratio of primary to secondary reaction rates under different cooling conditions.

The primary reactions, oxygen reactions, MH formation, and Joule heating contribute to the total heat generation rate, as described by Eq. 29. Figure 7 also displays these contributions of heat generation in the Ni-MH cell for h = 5 W/m^2 K. Initially, the heat effect due to primary reactions offsets that due to MH formation, while the oxygen reactions are insignificant and the Joule heating negligible. With time, the heat absorbed by the primary reactions decreases because of the reduction in their enthalpy potentials (*i.e.*, $U_j - T\,\partial U_j/\partial T$) [32,40] and the heat generated from the metal hydride formation remains constant. As a result, the total heat generation rate gradually increases. When the cell is being charged upon a condition at which the oxygen reactions become significant, the total heat generation rate increases dramatically because the enthalpy potentials of oxygen reactions are comparatively large and the heat absorbed by the primary reactions is negligibly small. When the cell is being overcharged at a rate as large as 1C, almost all the current applied to the cell is used to generate oxygen at the positive electrode and only a portion of oxygen can be reduced at the negative electrode. In other words, the primary reaction at the MH electrode still accounts for a large portion of applied current due to the presence of designated overcharge reserve, as indicated in Fig. 7 by the heat effect due to MH formation. The net heat generation rate is large, but steady state is reached because of a constant reaction rate.

Figure 8 shows the variations in reaction currents during 1C charging. Initially, the oxygen reaction is negligible, and all the current applied to the cell is used to convert the active materials from the discharged to charged state. The oxygen reactions become significant when the charge input exceeds 90% of nominal cell capacity. It is obvious that the oxygen reaction current increases and the primary reaction current decreases, with the total current remaining the same. The charge acceptance, defined as the ratio of primary reaction current to the total current, then exactly follows the curves of primary reaction current, with a maximum value of 100%. Apparently, the heat dissipation rate affects the charge acceptance only after 100% of cell nominal capacity is applied. The worse the heat dissipation, the smaller the charge acceptance.

Thermal effects during float charging.—In addition to the constant-current charging mode, float charging at a constant voltage is also frequently applied to Ni-MH batteries. Figure 9 shows the reaction currents when a constant voltage of 1.5 V is applied to the Ni-

S0013-4651(00)02-015-2 CCC: $7.00

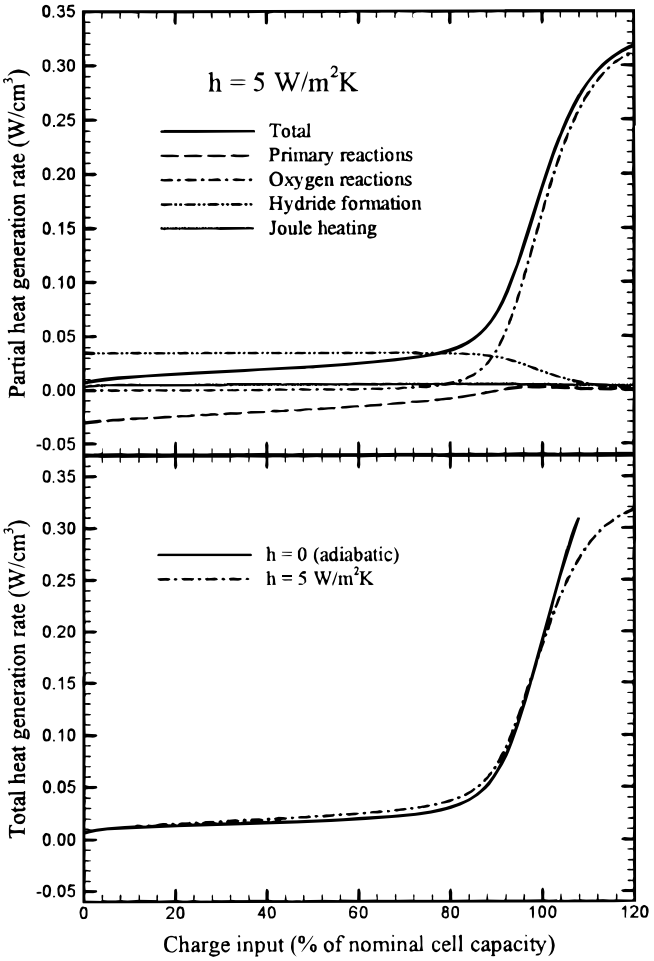

Figure 7. Total and partial heat generation rates during 1C charging under various thermal conditions. The partial heat generation rates are defined by Eq. 61–64.

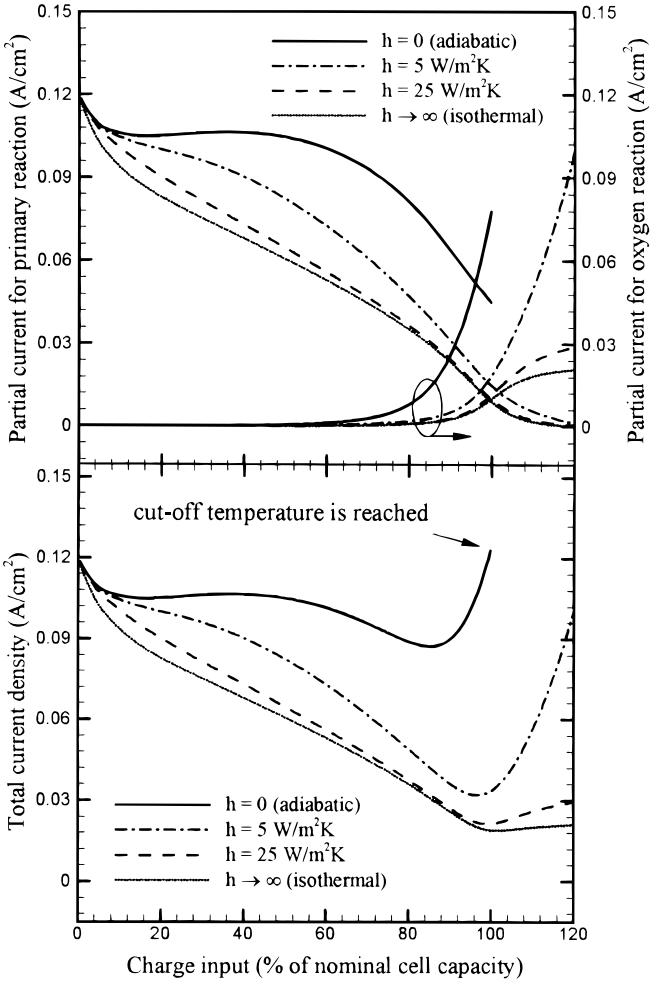

Figure 9. Reaction currents during 1.5 V float charging under various thermal conditions.

MH cell. The current due to oxygen reactions is negligible when the charge input is less than 60% of nominal cell capacity in all cases. A poorer cooling condition causes an earlier occurrence of oxygen reactions resulting from the higher cell temperature. The current due to primary reactions decreases very quickly during the first 10% of nominal cell capacity because the surface overpotential, the driving force for the electrochemical reactions, drops quickly due to the continual increase of the electrode OCPs during charging. The primary reaction current is strongly affected by cooling conditions. The higher the heat dissipation rate, the lower the cell temperature, and hence the lower reaction current. The reaction current increases even after the initial quick drop, indicating that the reactions are facile at high temperatures. The total reaction current from both primary and oxygen reactions is expected to have a minimum value when both the primary and oxygen reaction currents are small. A lower steady total current can be obtained at a higher heat dissipation rate.

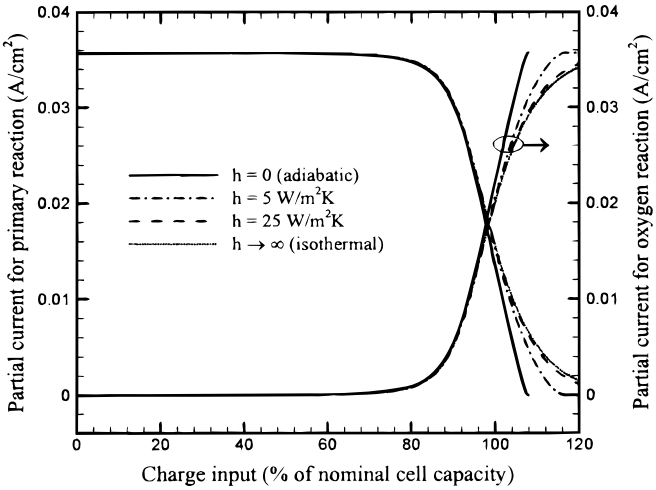

Figure 8. Primary and oxygen reaction currents at nickel positive electrode during 1C charging under various thermal conditions. The partial currents are defined by Eq. 65 and 66.

Figure 10 shows the cell temperature and pressure variations during 1.5 V float charging. The cell temperature is strongly affected by the cooling condition. While the cell temperature continues to increase under poor cooling conditions, it decreases continuously after an initial quick rise. The larger the heat-transfer coefficient, the earlier the decrease occurs. This decrease in cell temperature is arrested when the cell is near its fully charged state and oxygen reactions become dominant. The cell temperature then increases drastically, the magnitude of which depends on the cooling condition. While the cell temperature tends to approach a constant value at high cooling rates, the cell virtually underegoes thermal runaway at low cooling rates.

The oxygen reactions contribute to the cell pressure buildup. The earlier the oxygen reactions take place, the more the cell pressure builds up. While the cell pressure can be maintained at a low level when the heat dissipation rate is high and hence the cell temperature is low, it builds up so quickly under poor cooling conditions that safety becomes a concern.

S0013-4651(00)02-015-2 CCC: $7.00

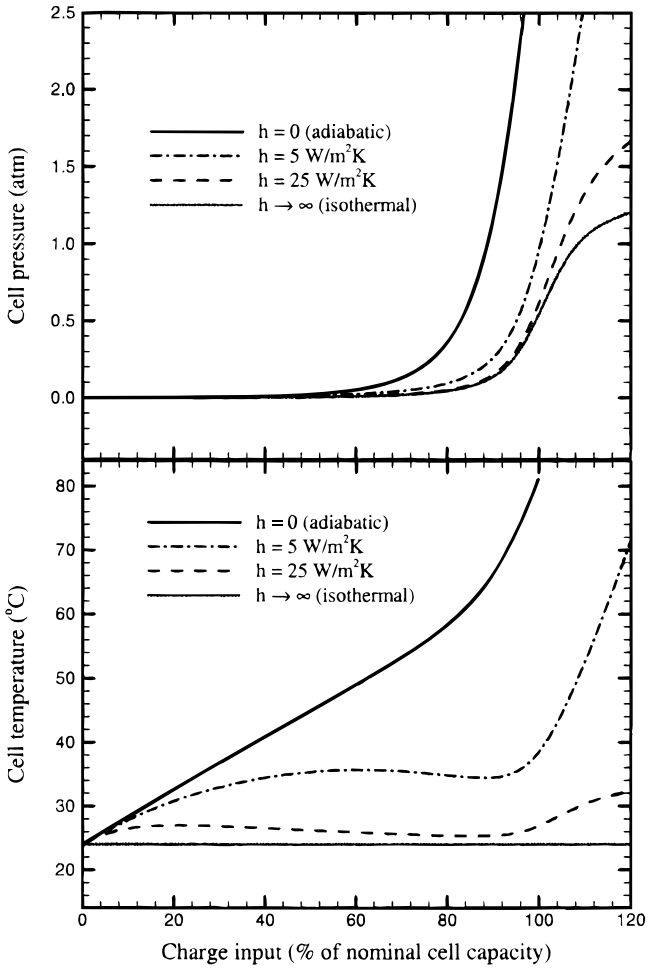

Figure 10. Cell temperature and pressure evolutions during 1.5 V float charging under various thermal conditions.

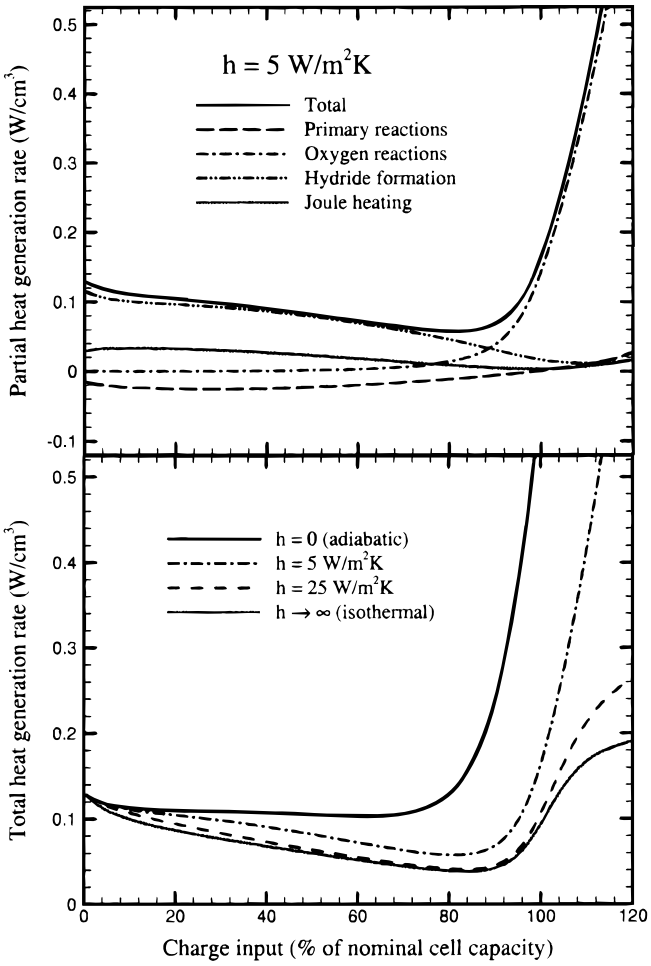

Figure 11. Total and partial heat generation rates during 1.5 V float charging under various thermal conditions.

As found earlier, the heat generation rate of the cell is nearly independent of thermal conditions during constant-current charging. This is not the case during float charging. Figure 11 displays the heat generation rates of the Ni-MH cell during 1.5 V float charging. The total heat generation rate continues to decrease before the oxygen reactions, which result in a dramatic increase in the total heat generation rate, become significant. It decreases more quickly at a larger heat dissipation rate. The smallest heat generation rate occurs when the heat dissipation rate is infinitely large and the cell is accordingly isothermal. When the cell is adiabatic, the heat generation rate is nearly constant after an initial quick drop.

Figure 11 also shows the partial heat generation rates that contribute to the total rate for $h = 5$ W/m^2 K. The heat effect due to the hydride formation is dominant when the charge input is below 80% of nominal cell capacity, whereas the heat effect due to the oxygen reactions is dominant when the charge input is larger than 95% of nominal cell capacity. The heat effect due to Joule heating experiences a minimum close to 100%, indicating that total current due to both primary and oxygen reactions has a minimum value there. The heat effect due to MH formation decreases gradually with time and reaches a minimum at a charge input of ~110% of nominal cell capacity, meaning that the primary reaction still proceeds at the MH electrode and is facile due to the increase in the cell temperature. As a result, the heat effect due to the primary reactions at both nickel and MH electrodes increases with increasing oxygen reactions.

Figure 12 shows the effect of thermal conditions on the charge acceptance of the Ni-MH cell during 1.5 V float charging. The charge acceptance reflects the efficiency of the charging process. The difference in the charge acceptance is indiscernible for all cases when the charge input is less than 60% of nominal cell capacity. However, it drops quickly as soon as the oxygen reactions become significant. When the charge input reaches 120% of nominal cell

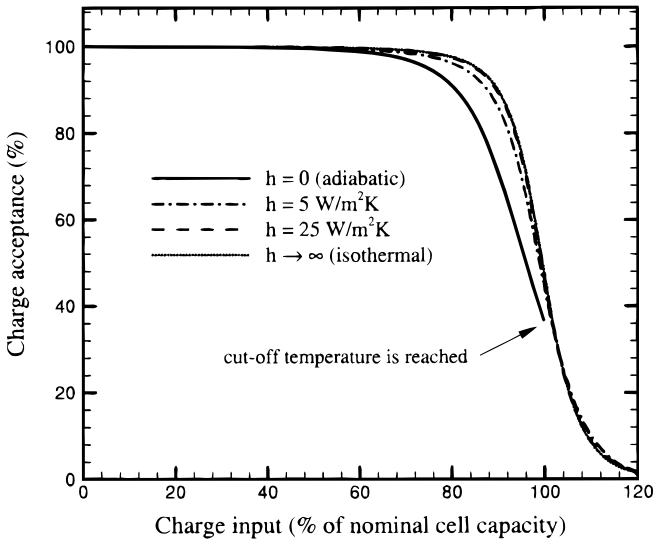

Figure 12. Charge acceptance during 1.5 V float charging under various thermal conditions.

S0013-4651(00)02-015-2 CCC: $7.00

capacity, the charge acceptance virtually disappears. The oxygen reaction is much more facile at a higher cell temperature that results from a poorer cooling condition. Accordingly, the charge acceptance drops earlier when the heat-transfer coefficient is smaller. This behavior is different from that displayed in Fig. 8 during 1C charging.

Conclusions

A general thermal energy equation has been derived using the volume-averaging technique, along with a local heat generation rate resulting from electrochemical reactions, phase transformation, and Joule heating. The thermal model is fully coupled to the micro-macroscopic electrochemical model previously developed via temperature-dependent physicochemical properties. The thermal-electrochemical coupled model is multidimensional and capable of predicting the temperature distribution inside a cell in addition to the average cell temperature, thus providing a cost-effective tool to accurately predict the cell electrochemical and thermal behaviors, and most important, to identify the mechanisms responsible for thermal runaway.

Numerical simulations were performed to illustrate the significance of thermal and electrochemical coupling. The electrochemical and thermal behaviors of a Ni-MH battery were then explored numerically using the fully coupled thermal-electrochemical model. Various operation modes and thermal conditions were examined. The cell temperature rise is significant when the cell is charged at high rates and under poor cooling conditions, primarily due to the oxygen reactions occurring near the end of full charge. The cell thermal behavior during constant-current charging was found to differ significantly from that during float charging.

Work is underway to examine the predictablity of the present model for hot spots within a cell. The thermal effect on the active material degradation and hence battery cycle life will be incorporated in future work.

Acknowledgment

This work was supported, in part, by the Defense Advanced Research Projects Agency (DARPA), Tactical Technology Office, Electric and Hybrid Vehicle Technology Program, under cooperative agreement no. MDA 972-95-2-0009 and 972-95-3-0019.

The Pennsylvania State university assisted in meeting the publication costs of this article.

Appendix

An Order-of-Magnitude Estimate of the First Term in Eq. 20

The first term in Eq. 20, Q_k^{joule}, represents the Joule heating rate due to fluctuations at the microscopic level. It can be rewritten as

$$\text{1st term in Eq. 20} = -\frac{<i_k>}{\epsilon_k} a_{km}\left(\overline{\phi}_{km} - <\phi_k>^k\right) \qquad \text{[A-1]}$$

Note that the microscopic ohmic drop can be estimated from the transfer current density normal to the electrode/electrolyte interface as follows

$$\overline{\phi}_{km} - <\phi_k>^k \sim \frac{r_s}{\sigma_k} \sum_j \bar{i}_{nj} \qquad \text{[A-2]}$$

where r_s is the microscopic length scale (or the particle radius). Substituting Eq. A-2 into A-1 results in

$$\text{1st term in Eq. 20} \sim -\frac{<\mathbf{i}_k>}{\epsilon_k\sigma_k} r_s a_{se} \sum_j \bar{i}_{nj} = \frac{\sigma_k^{eff}\nabla<\phi_k>^k}{\epsilon_k\sigma_k} r_s a_{se} \sum_j \bar{i}_{nj} \qquad \text{[A-3]}$$

where use has been made of the volume-averaged Ohm's law, Eq. 32. Furthermore, it follows from the conservation of charge over an entire electrode that

$$a_{se} \sum_j \bar{i}_{nj} \sim \frac{<i_k>}{L_e} \qquad \text{[A-4]}$$

where L_e is the macroscopic thickness of the electrode. Substituting Eq. A-4 into A-3 and comparing this term to the macroscopic Joule heating rate yields

$$\frac{\text{1st term in Eq. 20}}{-<i_k>\cdot\nabla<\phi_k>^k} \sim \frac{\sigma_k^{eff}}{\epsilon_k\sigma_k}\frac{r_s}{L_e} \sim \frac{r_s}{L_e} << 1 \qquad \text{[A-5]}$$

since the ratio of micro to macro length scales is much smaller than unity.

List of Symbols

A	projected electrode area, cm^2
A_c	surface area through which heat is removed from the cell, cm^2
a	activity of a species
a_{sj}	specific surface area active for electrode reaction j, cm^2/cm^3
c_i	volume-averaged concentration of species i over a phase, mol/cm^3
c_p	specific heat, J/kg K
D^i	diffusion coefficient of species i, cm^2/s
E_{act}	activation energy, J/mol
F	Faraday's constant, 96,487 C/mol
$\hat{H}$	partial molar enthalpy of a species, J/mol
h	enthalpy of species participating in the phase transformation, J/mol
h	equivalent heat-transfer coefficient, W/cm^2 K
I	volumetric current, A/cm^3
$\mathbf{i}$	current density vector, A/cm^2
i	applied current density, A/cm^2
$\bar{i}_{nj}$	transfer current density of reaction j, A/cm^2
$\mathbf{J}$	molar flux of a species, mol/cm^2 s
J_{eg}^{O2}	mass-transfer rate of oxygen across gas/electrolyte interface, mol/cm^3 s
j^i	reaction current resulting in production or consumption of species i, A/cm^3
L	cell width, cm
L_e	electrode thickness, cm
l_{se}	microscopic diffusion length of species in a solid phase, cm
n_j	number of electrons transferred in reaction j
Q	volumetric heat removal rate from the cell, J/cm^3 s
Q_k^{Joule}	microscopic Joule heating term due to electrical nonequilibrium, J/cm^3 s
Q_{km}^{d}	interfacial heat-transfer rate due to conduction, J/cm^3 s
Q_{km}^{Γ}	thermal effect due to the interface movement, J/cm^3 s
$\mathbf{q}$	heat flux, J/cm^2 s
q	volumetric heat generation rate, J/cm^3 s
R	universal gas constant, 8.3143 J/mol K
R_o	applied load, Ω
R_{sb}, R_{se}	area-specific electrical resistance across the solid/substrate interface, Ω cm^2
$\hat{S}$	partial molar entropy, J/mol K
s_j	stoichiometric coefficient of a species involved in reaction j
T	absolute temperature of the cell system, K
t	time, s
t_-^o	transference number of OH^- with respect to the solvent velocity
U_j	open-circuit potential of electrode reaction j, V
V	applied voltage, V
V_c	cell volume, cm^3
V_g	volume occupied by the gas phase, cm^3
$\mathbf{v}$	velocity vector, cm/s
$\mathbf{w}$	interface velocity vector, cm/s
x	coordinate along the cell width, cm
z	charge number of an ionic species

Greek

ϵ	volume fraction of a phase
η_j	surface overpotential of electrode reaction j, V
Π_j	the Peltier coefficient, V
$\mathbf{\Gamma}$	phase transformation rate, mol/cm^2 s
κ	conductivity of an electrolyte, S/cm
κ_D	diffusional conductivity of a species, A/cm
ρ	density, g/cm^3
σ	conductivity of solid active material, S/cm
λ	thermal conductivity, W/cm K
μ	electrochemical potential of a species, J/mol
μ^o	standard chemical potential of a species, J/mol
Δh^*	enthalpy change due to phase transformation, J/mol
ϕ	potential in a phase, V
$\bar{\phi}$	surface potential in a phase, V

Subscript

b	substrate
e	electrolyte phase
eff	effective
eg	electrolyte/gas interface
g	gas phase
hyd	hydride formation

S0013-4651(00)02-015-2 CCC: $7.00

km	interface between phases k and m
MH	metal hydride active material
Ni	nickel active material
ref	with respect to a reference state
s	solid phase
sb	solid/substrate interface
se	solid/electrolyte interface
sep	separator
o	initial value

Superscript

av	average
eff	effective
H	species hydrogen or proton
H_2O	solvent water
OH	species OH^-
—	overbar, average over an interface

References

1. C. Y. Wang, W. B. Gu, and B. Y. Liaw, *J. Electrochem. Soc.*, **145**, 3407 (1998).
2. W. B. Gu, C. Y. Wang, S. L. Li, B. Y. Liaw, and M. M. Geng, *Electrochim. Acta*, **44**, 4525 (1999).
3. T. F. Fuller and J. Newman, in *Modern Aspects of Electrochemistry*, Vol. 27, R. E. White, J. Bockris, and B. Conway, Editors, p. 359, Plenum Press, New York (1995).
4. G. Zheng, B. N. Popov, and R. E. White, *J. Appl. Electrochem.*, **27**, 1328 (1997).
5. D. Berndt and E. Meissner, *INTELEC'90—Proceedings of 12th International Telecommunications Energy Conference*, p. 148 (1990).
6. D. Pavlov, *J. Power Sources*, **64**, 131 (1997).
7. C. R. Pals and J. Newman, *J. Electrochem. Soc.*, **142**, 3274, 3282 (1995).
8. Y. Chen and J. W. Evans, *J. Electrochem. Soc.*, **143**, 2708 (1996).
9. F. Joubert, J. Bouet, and J.-F. Fauvarque, in *Batteries for Portable Applications and Electric Vehicles*, C. F. Holmes and A. R. Landgrebe, Editors, PV 97-18, p. 837, The Electrochemical Society Proceedings Series, Pennington, NJ (1997).
10. M. S. Wu, Y. Y. Wang, and C. C. Wan, *J. Power Sources*, **74**, 202 (1998).
11. Z. L. Zhang, M. H. Zhong, F. M. Liu, F. P. Zhong, and F. Wu, *J. Power Sources*, **70**, 276 (1998).
12. J. Lee, in *Electrochemical and Thermal Modeling of Battery, Fuel cell, and Photoenergy Conversion Systems*, J. R. Selman and H. C. Maru, Editors, PV 86-12, p. 206, The Electrochemical Society Proceedings Series, Pennington, NJ (1986).
13. J. Newman and W. Tiedemann, *J. Electrochem. Soc.*, **142**, 1054 (1995).
14. K. W. Choi and N. P. Yao, *J. Electrochem. Soc.*, **126**, 1321 (1979).
15. J. Lee, K. W. Choi, N. P. Yao, and C. C. Christianson, *J. Electrochem. Soc.*, **133**, 1286 (1986).
16. H. Huang and T. V. Nguyen, *J. Electrochem. Soc.*, **144**, 2062 (1997).
17. J. Kim, T. V. Nguyen, and R. E. White, *J. Electrochem. Soc.*, **139**, 2781 (1992).
18. Y. Chen and J. W. Evans, *J. Electrochem. Soc.*, **140**, 1833 (1993).
19. Y. Chen and J. W. Evans, *J. Electrochem. Soc.*, **141**, 2947 (1994).
20. Y. Chen and J. W. Evans, *Electrochim. Acta*, **39**, 517 (1994).
21. M. K. Verbrugge *AIChE J.*, **41**, 1550 (1995).
22. Y. Chen and J. W. Evans, *INTELEC'96–Proceedings of the 18th International Telecommunications Energy Conference*, p. 1465 (1996).
23. W. Tiedemann and J. Newman, in *Battery Design and Optimization*, S. Gross, Editor, PV 79-1, p. 23, The Electrochemical Society Proceedings Series, Pennington, NJ (1979).
24. W. Tiedemann and J. Newman, in *Advances in Lead-Acid Batteries*, K. R. Bullock and D. Pavlov, Editors, PV 84-14, p. 336, The Electrochemical Society Proceedings Series, Pennington, NJ (1984).
25. H. Huang and T. V. Nguyen, *J. Electrochem. Soc.*, **144**, 2420 (1997).
26. J. Kim, T. V. Nguyen, and R. E. White, *J. Electrochem. Soc.*, **141**, 333 (1994).
27. P. De Vidts, J. Delgado, B. Wu, D. See, K. Kosanovicb, and R. E. White, *J. Electrochem. Soc.*, **145**, 3874 (1998).
28. C. R. Pals, M. Doyle, T. F. Fuller, and J. Newman, in *Douglas N. Bennion Memorial Symposium*, R. E. White and J. Newman, Editors, PV 94-22, p. 248, The Electrochemical Society Proceedings Series, Pennington, NJ (1994).
29. M. Doyle and J. Newman, *Electrochim. Acta*, **40**, 2191 (1995).
30. G. G. Botte, B. A. Johnson, and R. E. White, *J. Electrochem. Soc.*, **146**, 914 (1999).
31. D. Bernardi, E. Pawlikowski, and J. Newman, *J. Electrochem. Soc.*, **132**, 5 (1985).
32. L. Rao and J. Newman, *J. Electrochem. Soc.*, **144**, 2697 (1997).
33. R. B. Bird, W. E. Stewart, and E. N. Lightfoot, *Transport Phenomena*, John Wiley & Sons, New York (1960).
34. J. Newman, *Electrochemical Systems*, Prentice-Hall, Englewood Cliffs, NJ (1991).
35. J. Newman, *Ind. Eng. Chem. Res.*, **34**, 3208 (1995).
36. Y. V. Kuzminskii, L. I. Nykova, and A. A. Andriiko, *J. Power Sources*, **46**, 29 (1993).
37. Y. V. Kuzminskii and A. V. Gorodyskii, *J. Electroanal. Chem.*, **252**, 21 (1988).
38. M. J. Lampinen and M. Fomino, *J. Electrochem. Soc.*, **140**, 3537 (1993).
39. Q. Xu, S. Kjelstrup, and B. Hafskjold, *Electrochim. Acta*, **43**, 2597 (1998).
40. H. F. Gibbard, *J. Electrochem. Soc.*, **125**, 353 (1978).
41. D. Berndt, *Maintenance-Free Batteries Lead-acid, Nickel/Cadmium, Nickel/Hydride*, John Wiley & Sons, New York (1993).
42. B. Paxton and J. Newman, *J. Electrochem. Soc.*, **144**, 3818 (1997).
43. D. Ohlendorf and H. E. Flotow, *J. Less-Common. Met.*, **73**, 25 (1980).
44. S. G. Bratsch, *J. Phys. Chem. Ref. Data*, **18**, 1 (1989).
45. B. V. Ratnakumar, P. Timmerman, C. Sanchez, S. Di Stefano, and G. Halpert, *J. Electrochem. Soc.*, **143**, 803 (1996).
46. Y. Okinaka, *J. Electrochem. Soc.*, **117**, 289 (1970).
47. R. E. Davis, G. L. Horvath, and C. W. Tobias, *Electrochim. Acta*, **12**, 287 (1967).
48. D. M. MacArthur, *J. Electrochem. Soc.*, **117**, 729 (1970).
49. W. B. Gu and C. Y. Wang, in *Lithium Batteries*, R. A. Marsh, Z. Ogumi, J. Prakash, and S. Surampudi, Editors, PV 99-25, p. 748, The Electrochemical Society Proceedings Series, Pennington, NJ (1999).